

# Estimation of Input Function from Dynamic PET Brain Data Using Bayesian Blind Source Separation

Ondřej Tichý and Václav Šmídl

Institute of Information Theory and Automation,  
Pod Vodárenskou Věží 4, Prague, Czech republic  
{otichy,smidl}@utia.cas.cz

**Abstract.** Selection of regions of interest in an image sequence is a typical prerequisite step for estimation of time-activity curves in dynamic positron emission tomography (PET). This procedure is done manually by a human operator and therefore suffers from subjective errors. Another such problem is to estimate the input function. It can be measured from arterial blood or it can be searched for a vascular structure on the images which is hard to be done, unreliable, and often impossible. In this study, we focus on blind source separation methods with no needs of manual interaction. Recently, we developed sparse blind source separation and deconvolution (S-BSS-vecDC) method for separation of original sources from dynamic medical data based on probability modeling and Variational Bayes approximation methodology. In this paper, we extend this method and we apply the methods on dynamic brain PET data and application and comparison of derived algorithms with those of similar assumptions are given. The S-BSS-vecDC algorithm is publicly available for download.

**Keywords:** blind source separation, variational Bayes method, dynamic PET, input function, deconvolution

## 1. Introduction

Physical examination using scintigraphy [6] or positron emission tomography (PET) [11] allows us to see processes inside the living body without surgery. Contrast medium can be applied into the body and its spatial distribution can be measured for the selected part of body. In PET, the measured activity in each voxel is a superposition of the signal tissues. Since the measurement is done repetitively, a time distribution of the scanned region of body can be obtained. The task of medical analysis is to obtain the clear activity of each tissue separately.

In practice, the analysis of dynamic PET is often based on the knowledge of input function (IF), i.e. activity of the medium in the blood [22]. This can be achieved using arterial blood sampling [10] which is very invasive and sensitive to errors. A number of methods has been proposed to lower invasiveness of measurement [5] or derive the IF directly from the dynamic PET images. In some cases, blood structure can be directly observed on the images. In this cases, a region of interest (ROI) can be manually placed on vascular structures and its related time-activity curve (TAC) can be obtained [8]. Manual selection of the ROIs may suffer from subjectivity. This issues has been addressed using e.g. automatic clustering methods [19].

However, more important problem is that the selected blood structure typically accumulate activity not only from the blood but also from other tissues; hence, a mixture of TACs is obtained instead of the pure IF. Moreover, such a structure is often not present on scanned images and no such ROI with pure IF can be placed. Separation of mixed signals in general is the task for blind source separation (BSS) methods. They offer an automatic way for separation of tissues from the measured sequence. Some methods are general with no extra medical assumptions [21,3] and provide non-negative matrix factorization essentially [17,7]. Medically motivated extensions have been proposed based on compartmental modeling [23,31] where detailed model of the tracer behavior is incorporated into the separation procedure.

Recently, we have studied the influence of the sparsity assumption on BSS problems, which means to reflect that the activity of each source is present only on limited region of recorded images [14]. We developed sparsity in blind source separation and deconvolution (S-BSS-vecDC) method [29] which assumes each TAC to be the results of a convolution between common input function and source-specific convolution kernel and source-images to be sparse. The sparsity is not strict but favored by proposed probabilistic model using automatic relevance determination principle [2]. Suitability of the S-BSS-vecDC algorithm was studied on dynamic PET in [28]. In this paper, we extend the comparison by adding a method that estimates the full covariance matrix of the convolution kernels using Wishart prior model [30].

We compare the proposed and existing methodology on the task of tissue separation of the TAC of the blood. Specifically, we analyze data from dynamic PET of a brain where structures with arterial blood are obvious and thus this data can be used as the simplest possible benchmark of separation methods. The comparison is performed for two cases: slice by slice processing and the whole volume processing. It allows us to study the separation performance as well as stability of the algorithms.

The structure of the paper follows. In Section 2, related work on blind source separation in context of dynamic PET data analysis is discussed. In Section 3, models for blind source separation are introduced, three classical models without any specific domain assumptions and three models with convolution assumption. Variational Bayes method for estimation of models parameters is described in the end of the Section. In Section 4, an experiment with dynamic PET brain data is conducted slice by slice and for the whole volume while the estimated blood sources are compared with the manually obtained estimate. In Section 5, discussion and conclusion are given.

## 2. Related Work

The input function is important parameter in quantitative analysis of dynamic PET studies. The input function is traditionally obtained from blood sampling [10] which is very invasive and often inappropriate in practice. A typical alternative practice is to select a ROI where clear blood or vascular structure is present and the TAC estimated from this region (after background correction) is assumed to be the input function. This step can be done manually or automatically [4,32]; however, such a structure may not be present in the images. Recently, attempts were made to extract image-derived input function as well [1,16]. All of these methods were reported to provide good results in specific conditions

and some of them are used by their authors but, again, none has been generally accepted in general clinical practice.

Promising model of dynamic PET images is the one where it is assumed that data are superposition of signals from several sources while each source image is weighted by its related time-activity curve. This model is the base for non-negative matrix factorization [17] which was already applied to PET data [3]. This model was improved using additional assumptions such as sparsity [13] or convolution assumption [24]; however, noise properties and unknown number of source remain issues. Similar model was proposed in [9] to solve near-separable non-negative matrix factorization where it is assumed that each source has at least one clear image in the data. This assumption is suitable for wide class of problems but limits this algorithm in medical data analysis. We tried to overcome these issues using Bayesian approach in [26] where sparsity of source images was modeled and in [31] where convolution assumption was incorporated and piece-wise linear convolution kernels was modeled. These algorithms provide good results in domain-specific tasks. To overcome dependency on domain, free-form approach was pioneered in [27] using automatic relevance determination principle [2] and S-BSS-vecDC algorithm was proposed in [29] where noise level as well as number of sources are estimated within Bayesian model and sparsity of source images and convolution model was incorporated using general, i.e. no domain-specific, assumptions. This algorithm will be tested and compare with other algorithms in this paper.

### 3. Blind Source Separation Methods

The general assumptions of the blind source separation methods, which is common for all methods to be compared, will be summarized. Then, we will make detailed views on the selected methods.

The observed data are assumed to arise as a superposition of signals from underlying tissues and the signal is assumed to be degraded by a noise. The data at each time  $t$  is stored columnwise in vector  $\mathbf{d}_t$ . Since the number of voxels is  $p$ ,  $\mathbf{d}_t \in \mathbf{R}^{p \times 1}$ . The vector  $\mathbf{d}_t$  is assumed to be an observation of a superposition of  $r$  tissue images stored in vectors  $\mathbf{a}_k \in \mathbf{R}^{p \times 1}$ ,  $k = 1, \dots, r$ . Each tissue image is weighted by its related TAC  $\mathbf{x}_k \in \mathbf{R}^{n \times 1}$ ,  $k = 1, \dots, r$ , where  $n$  is the number of measurements,  $t = 1, \dots, n$ . Summarizing the vectors into matrices  $D = [\mathbf{d}_1, \dots, \mathbf{d}_n] \in \mathbf{R}^{p \times n}$ ,  $A = [\mathbf{a}_1, \dots, \mathbf{a}_r] \in \mathbf{R}^{p \times r}$ , and  $X = [\mathbf{x}_1, \dots, \mathbf{x}_r] \in \mathbf{R}^{n \times r}$ , the matrix formulation of the superposition problem can be written as

$$D = AX^T + E. \quad (1)$$

Here  $()^T$  denotes transpose of a matrix or vector and  $E$  is the noise matrix of the same size as the data matrix  $D$ .

#### 3.1. Non-negative Matrix Factorization

Non-negative matrix factorization (NMF) assumes that the data matrix  $D \in \mathbf{R}^{p \times n}$  can be approximated by linear combination  $D \approx AX^T$ , where  $A \in \mathbf{R}_+^{p \times r}$ , and  $X \in \mathbf{R}_+^{n \times r}$  is TACs recovering the columns of  $D$  using the columns of  $A$ . The number of sources,  $r$ , has to be given. We consider the version of the NMF algorithm [3] with the Euclidean

distance measuring the quality of the approximation of the matrices  $D$  by the product  $AX^T$  defined as

$$\|D - AX^T\|_2 = \sum_{i,j} (D_{ij} - (AX^T)_{ij})^2, \quad (2)$$

where the convergence to a local optimum is guaranteed [18].

### 3.2. Blind Source Separation with Positivity

Additional biologically-motivated assumptions are imposed on the elements of (1) in the probabilistic model of Blind Source Separation with Positivity (BSS+): (i) all elements of the observed vectors  $\mathbf{d}_t$  are positive, (ii) all elements of the tissue images  $\mathbf{a}_k$  and the TACs  $\mathbf{x}_k$  are also positive, and (iii) the number of relevant sources,  $r$ , is unknown. These assumptions are translated into probabilistic model as described in [21]. Moreover, the variance of noise is estimated as well as the relevant number of vectors,  $r$ , using automatic relevance determination (ARD) mechanism [2].

### 3.3. Factor Analysis with Integrated Regions of Interests

The Factor Analysis with Integrated Regions of Interests (FAROI) method [26] has the same advantage as BSS+ method; however, tissue images are modeled in more detail. Each element of matrix  $A$ ,  $a_{i,k}$ , has indicator  $\mathbf{i}_{i,k}$  such as

$$\mathbf{i}_{i,k} = \begin{cases} 1 & \text{i-th pixel belongs to the k-th tissue} \\ 0 & \text{i-th pixel not belongs to the k-th tissue} \end{cases} \quad (3)$$

and then, the model for each pixel depends on the indicator as

$$f(a_{i,j}) = \begin{cases} \mathcal{U}(0, 1) & \mathbf{i}_{i,j} = 1, \\ t\mathcal{N}(0, \xi_j^{-1}, \langle 0, 1 \rangle) & \mathbf{i}_{i,j} = 0. \end{cases} \quad (4)$$

Here, uniform distribution  $\mathcal{U}(0, 1)$  is a model of the tissue and the truncated normal distribution  $t\mathcal{N}(0, \xi_j^{-1})$ , defined in Appendix A.1, models the noise around zero.

As a result, the FAROI model is capable to separate tissue images with small number of pixels which could be rejected as insignificant by the BSS+ model.

### 3.4. Blind Compartment Model Separation

The Blind Compartment Model Separation (BCMS) model [31] reflects that the TACs can be described by compartment model, where each TAC arise by a convolution between a common input function and a tissue-specific kernel [23,15]. Hence, each element of the matrix  $X$ ,  $x_{j,k}$ , is modeled as a convolution between the input function, vector  $\mathbf{b}$ , and the convolution kernel  $\mathbf{u}_k$  such as

$$x_{j,k} = \sum_{t=1}^j b_{j-t+1} u_{t,k}. \quad (5)$$

Since we define the matrix  $U = [\mathbf{u}_1, \dots, \mathbf{u}_r] \in \mathbf{R}^{n \times r}$  and the matrix  $B$  as

$$B = \begin{pmatrix} b_1 & 0 & 0 & 0 \\ b_2 & b_1 & 0 & 0 \\ \dots & b_2 & b_1 & 0 \\ b_n & \dots & b_2 & b_1 \end{pmatrix}, \quad (6)$$

the matrix  $X$  of all TACs can be rewritten as

$$X = BU, \quad (7)$$

and matrices  $U$  and  $B$  are now unknown parameters instead of the matrix  $X$ .

In the BCMS model, the input function  $\mathbf{b}$  is assured to be decreasing and kernels  $\mathbf{u}_k$  are assured to be decreasing and piece-wise linear with constant plateau in the beginning and the decreasing to zero [15]. All these assumption are formulated as prior distribution on model parameters and the model is solved using Variational Bayes method [25].

The limitation of BCMS method is its restrictive shape which is suitable only in limited number of situation such as in specific tasks in renal scintigraphy [31].

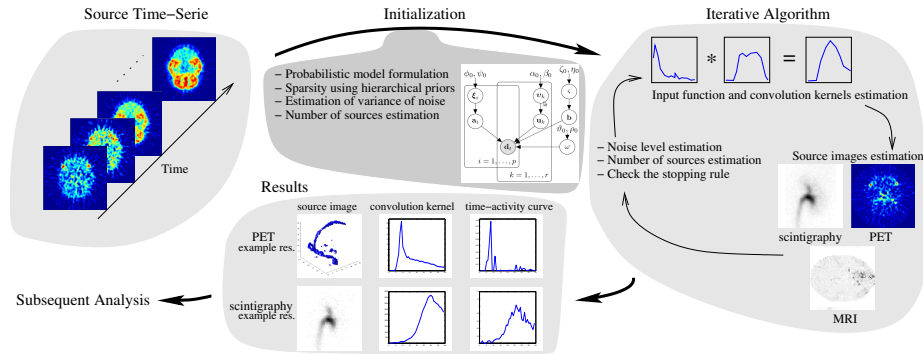


**Fig. 1.** The flowchart of the methods with incorporated convolution model.

### 3.5. Sparsity in Blind Source Separation and Deconvolution

Sparse Blind Source Separation and Deconvolution (S-BSS-vecDC) method [29] applies the automatic relevance determination (ARD) mechanism [2] to more variables of the model. The convolution model of TACs (7) is also adopted; however, in a more relaxed form than in the BCMS method. The convolutions kernels are not restricted to be in piece-wise linear form, the only imposed assumption is their sparsity via the ARD methodology:

$$f(u_{j,k}|v_{j,k}) = t\mathcal{N}(0, v_{j,k}^{-1}, [0; \infty]), \quad \forall j = 1, \dots, n, \quad (8)$$

$$f(v_{j,k}) = \mathcal{G}(\alpha_0, \beta_0). \quad (9)$$

Hence, each element of the convolution kernel is truncated to positive value, see Appendix A.1, and its variance  $v_{j,k}$  is modeled as a Gamma prior and estimated jointly with the convolution kernel.

The sparsity prior is also used for each element  $a_{i,k}$  of tissue images, matrix  $A$ , as

$$f(a_{i,k}|\xi_{i,k}) = t\mathcal{N}(0, \xi_{i,k}^{-1}, [0; 1]), \quad \forall i = 1, \dots, p, \quad (10)$$

$$f(\xi_{i,k}) = \mathcal{G}(\phi_0, \psi_0). \quad (11)$$

Note that in this case, the normal distribution (10) is truncated to real numbers from the interval  $[0; 1]$  which results in better stability of its solution.

The input function model is modeled as

$$f(\mathbf{b}|\varsigma) = t\mathcal{N}(\mathbf{0}_{n,1}, \varsigma^{-1}I_n), \quad f(\varsigma) = \mathcal{G}(\zeta_0, \eta_0), \quad (12)$$

where  $\varsigma$  is scaling parameter and  $\zeta_0, \eta_0$  are scalar chosen constants.

The probabilistic model is solved using Variational Bayes method [25]. The algorithm implemented in MATLAB can be downloaded from [http://www.utia.cas.cz/AS/softwaretools/image\\_sequences](http://www.utia.cas.cz/AS/softwaretools/image_sequences).

### 3.6. Blind Source Separation with Wishart Convolution Prior

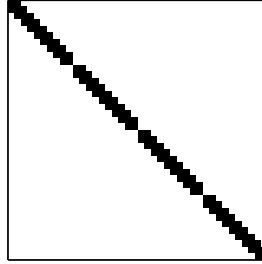


**Fig. 2.** The used localization matrix  $L$  in S-BSS-DW model. The black pixels denote ones and the white pixels denote zeros;  $n = 10$  and  $r = 4$ .

Fixed-form convolution kernels has been studied in Section 3.4 in BCMS method, and free-form sparse convolution kernels has been studied in Section 3.5 in S-BSS-vecDC method. In S-BSS-vecDC method, covariance matrix of convolution kernels is assumed to be diagonal in prior model (8). As an extension, we have studied a full prior covariance matrix of convolution kernels using Wishart distribution.

In vector notation, the convolution kernels are stored in one vector as  $\bar{\mathbf{u}} = \text{vec}(U) = \begin{pmatrix} \mathbf{u}_1 \\ \vdots \\ \mathbf{u}_r \end{pmatrix}$ . Note that then the S-BSS-vecDC model of  $\bar{\mathbf{u}}$  can be written as  $f(\bar{\mathbf{u}}|\mathbf{v}_1, \dots, \mathbf{v}_r) =$

$t\mathcal{N}(\mathbf{0}_{nr,1}, \text{diag}(\mathbf{v}_1, \dots, \mathbf{v}_r)^{-1})$ . The restriction of diagonal shape of the covariance matrix is here omitted using model

$$f(\bar{\mathbf{u}}|\mathcal{Y}) = t\mathcal{N}(\mathbf{0}_{nr,1}, \mathcal{Y}^{-1}), \quad (13)$$

where matrix  $\mathcal{Y} \in \mathbf{R}^{nr \times nr}$  is a full covariance matrix of vector  $\bar{\mathbf{u}}$  [30]. The matrix  $\mathcal{Y}$  is modeled as the Wishart distribution, see Appendix A.2,

$$f(\mathcal{Y}) = \mathcal{W}_{nr}(\alpha_0 I_{nr}, \beta_0), \quad (14)$$

with scalar prior parameters  $\alpha_0, \beta_0$ . The models of source images and the input function remain the same as given in equations (10)–(12).

Using this model, the full covariance matrix of the convolution kernels could be estimated; however, the model is then overparametrized since additional  $n^2 r^2$  parameters need to be estimated. To overcome this problem, we use an empirical observation that the most information is located in a few main diagonals of the covariance matrix. This approach is known as the localization and originates in data assimilation of atmospheric models [12]. Here, the estimate of the covariance matrix of the  $\bar{\mathbf{u}}, \hat{\mathcal{Y}}$ , is localized using the matrix  $L$  of the same size as

$$\hat{\mathcal{Y}}_{\text{loc}} = \hat{\mathcal{Y}} \circ L, \quad (15)$$

where symbol  $\circ$  denotes the Hadamard product, also known as the element-wise product, and the matrix  $L$  is defined in Figure 2. Theoretically, we can construct any conceivable matrix  $L$ ; however, the matrix for preservation of the three main diagonals is used in this study.

Once again, the probabilistic model is solved using Variational Bayes method [25]. The method is called Sparse Blind Source Separation and Deconvolution with Wishart Prior (S-BSS-DW). The flowchart of the methods with convolution model (BCMS, S-BSS-vecDC, and S-BSS-DW) is illustrated in Figure 1.

### 3.7. Approximate Variational Bayes Solutions

Estimation procedure for each prior model is derived using the Variational Bayes method [25]. The key step of the method is a replacement of intractable evaluation of joint posterior distribution by an approximate conditional independent distributions such as

$$f(A, \mathbf{b}, \bar{\mathbf{u}}, \omega|D) \approx f(A|D)f(\mathbf{b}|D)f(\bar{\mathbf{u}}|D)f(\omega|D), \quad (16)$$

where this example is for a model with convolution model of TACs. Following this methodology, shaping parameters of posterior distributions of model parameters are found using iterative procedure solving a set of derived implicit equations. The scheme of the methods with convolution model (BCMS, S-BSS-vecDC, S-BSS-DW) is shown in Figure 1.

## 4. Experiments

We will demonstrate the separation ability of the compared algorithms on a real brain data from dynamic PET available from [19].

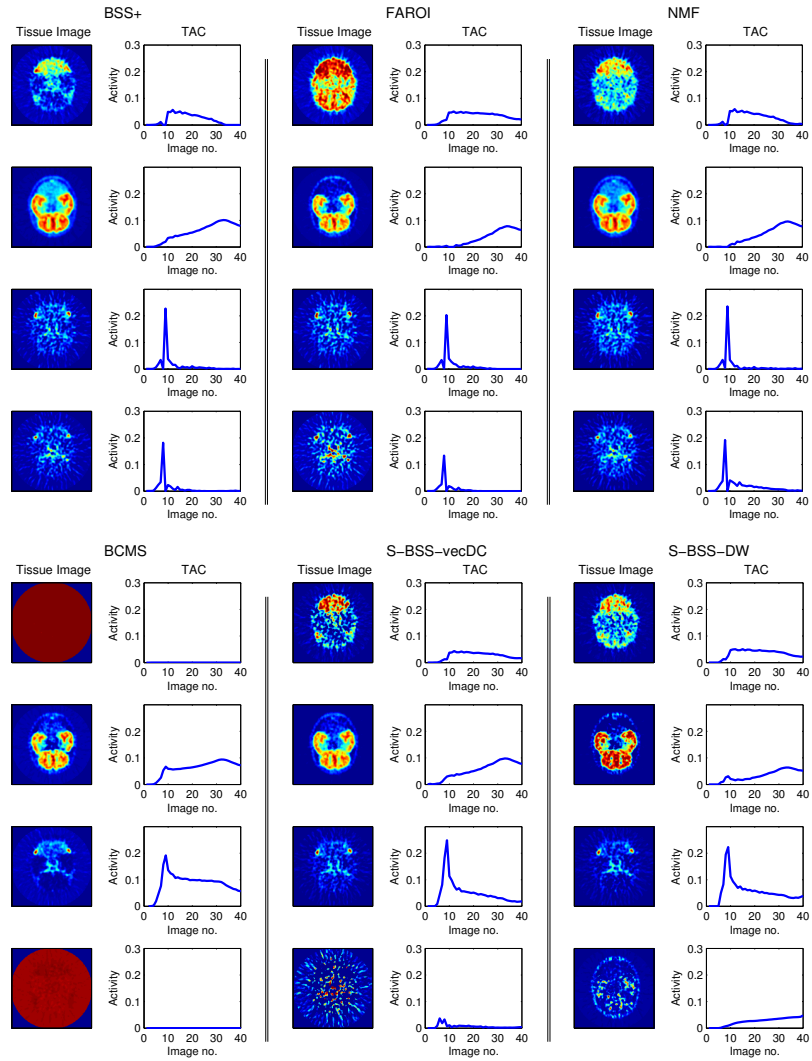


**Fig. 3.** The example results from the BSS+, FAROI, BCMS, NMF, S-BSS-vecDC, and S-BSS-DW algorithms are shown using sequence from the 10th slice. The estimated tissue images are in the left column and the estimated TACs are in the right column.



In this study,  $^{18}\text{F}$ -altanserin was applied to a patient and scanned with an 18-ring GE-Advance scanner (General Electric Medical System, Milwaukee, WI, USA) which is able to record 3D scans. Each scan consists of 35 image slices with an interslice distance 4.25 mm. The data were reconstructed into a sequence of  $128 \times 128 \times 35$  voxel matrices,  $2 \times 2 \times 4.25$  mm each voxel, using software provided by the manufacturer. The sequence consists of 40 voxel matrices,  $n = 40$ . For illustration of the method, we selected the 10th slice; however all algorithms can proceed the full volume.

Separation of the tissue images on the 10th slice using BSS+, FAROI, BCMS, NMF, S-BSS-vecDC, and S-BSS-DW algorithms are displayed in Figure 3 with  $r = 4$ . Note that the tissues separated by the S-BSS-vecDC algorithm have better anatomical meaning than those from the competing methods. The first tissue is clearly separated by the S-BSS-vecDC and S-BSS-DW algorithms while there is a residual activity from arterial veins by the BSS+ and the FAROI algorithms and from both, arterial veins and the second tissue, by the NMF algorithm. The BCMS algorithm was not able to separate the first tissue. The third tissue, arterial veins, is again clearly separated by the S-BSS-vecDC and S-BSS-DW algorithms while the BSS+, the FAROI, and the NMF algorithms split the arterial veins into two tissues mixed with the artifacts of the PET reconstruction. The BCMS algorithm combines the first tissue into the third tissue which can be recognized from its TAC. Moreover, the S-BSS-vecDC algorithm clearly separated the PET reconstruction artifacts as the fourth estimate; hence, the previous three physiological tissues are cleared from these artifacts.

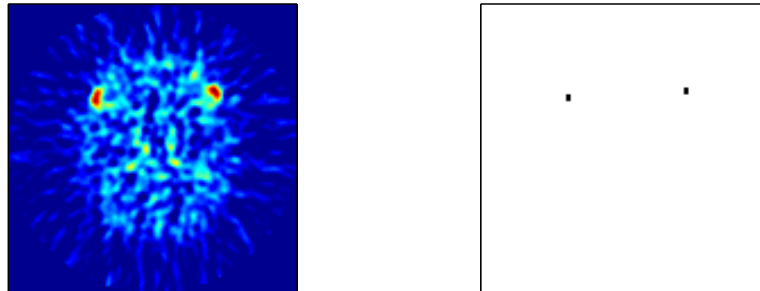


**Fig. 4.** The source image for  $n = 9$  is displayed on the left image. The manually selected ROIs of arterial veins are displayed on the right image.

Demonstration of the better separation is given using blood tissue where manual TAC can be easily obtain. First, we placed the ROI of the arterial veins on the tested sequence, see Figure 4. Second, comparison of the manual obtained blood TAC with those obtained using automatic method (Figure 3, the third row) is given in Figure 5. It can be observed that the S-BSS-vecDC and S-BSS-DW algorithms provide far closer TAC of the blood than other competing methods. In the next section, we provide sensitivity study of this result.

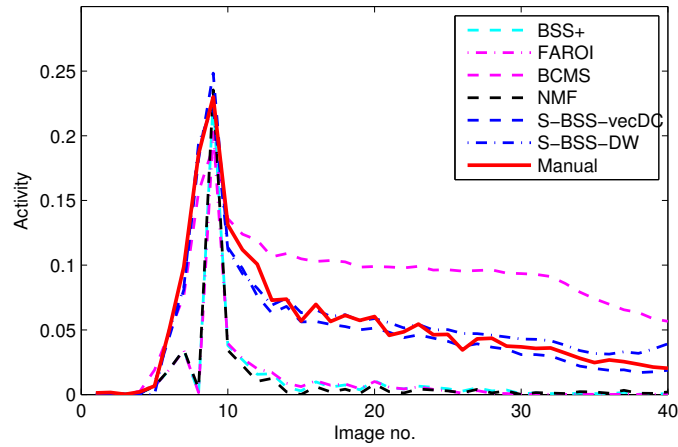


**Fig. 5.** Estimated TACs of blood tissue for the selected slice from all comparing methods are shown.

#### 4.1. Input Function Estimation from Slices

The goal of this experiment is to estimate input function from the whole measured volume.

Firstly, we created a manual ROI in several slices in the same sense as in Figure 4. We obtained a manually derived TAC of blood using this approach. Note that the TAC of the blood that was obtained manually is supposed to be slightly overestimated over the true blood curve since it contains signal from other tissues. This TAC will be used for comparison with the blood estimates from the BSS+, FAROI, NMF, and S-BSS-vecDC algorithm. Secondly, we ran the studied automatic algorithms on the whole volume slice by slice and the blood curves were selected from the results for each slice and for each algorithm. The results are displayed in Figure 6 using mean value and standard deviation at each time point. The curves are compared with manually obtained blood TAC, the red line.

The results in Figure 6 show that estimates from the S-BSS-vecDC algorithm are systematically closer to the manual method than estimates from any other algorithm. Note that the estimates from the S-BSS-DW algorithm are closer to those from the S-BSS-vecDC algorithm; however, there is deviation from the manual curve in the increasing part of the blood curve in the beginning of the activity. The small disproportion between manually obtained blood TAC and blood TAC from the S-BSS-vecDC algorithm is expected since manually selected ROI always contains other tissues and therefore accumulate activity from them.

#### 4.2. Input Function Estimation from the Whole Volume

The data matrix  $D$  is supposed to be  $D \in \mathbf{R}^{p \times n}$  where  $n$  is the time index. In previous experiments, we ran computations for each slice, hence, our  $p$  was  $128 \times 128$ . Here, we rearrange the data matrix for the whole volume at once so that  $p = 128 \times 128 \times 35$  and

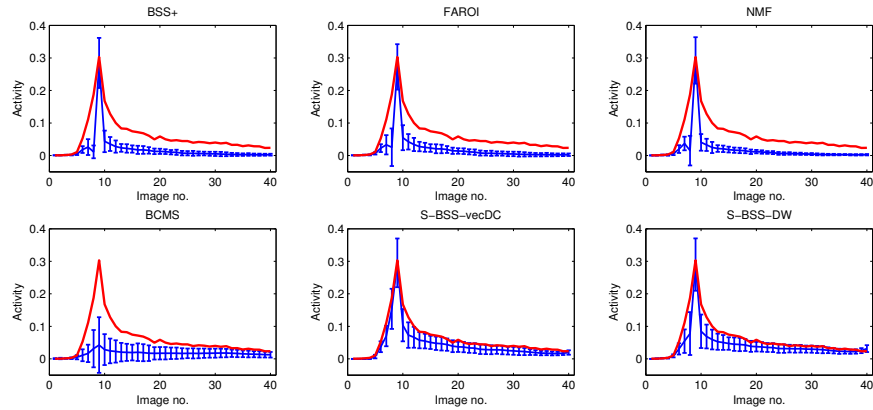


**Fig. 6.** The calculated mean and standard deviation of blood TAC for the BSS+, FAROI, NMF, BCMS, S-BSS-vecDC, and S-BSS-DW algorithms are displayed. The red curve is blood TAC obtained using manually placed ROI.

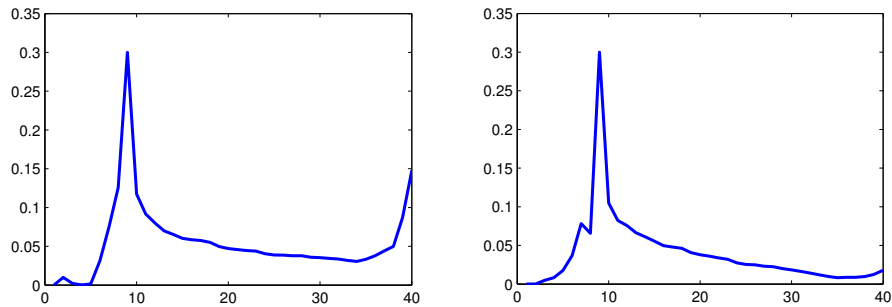


**Fig. 7.** Illustration of the boundary value problem observed for methods with convolution model of the TACs. **Left:** estimate of the blood TAC without data preprocessing. **Right:** with extension of the data.

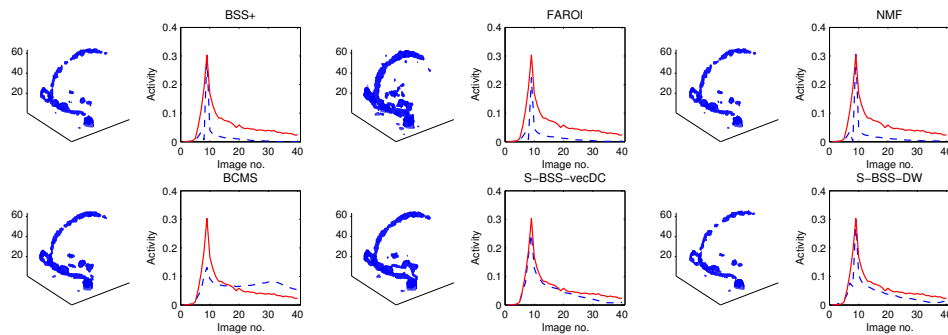


**Fig. 8.** Estimates of the blood tissue in the PET sequence composed of pixels belonging to the blood on the left and their time activity on the right. Results of the BSS+ (top left), FAROI (top middle), NMF (top right), BCMS (bottom left), S-BSS-vecDC (bottom middle), and S-BSS-DW (bottom right) algorithms from the full volume are shown. The red curve is the TAC of the blood obtained using manually placed ROI.

run the algorithms for the whole volume. We will study if the behavior of the TACs of the blood will vary from those obtained slice by slice.

Here, the boundary value problem known e.g. from deblurring in image processing [20] was observed by the models with incorporated convolution model of TACs, see example of this effect in Figure 7, left, where residual activity is observed at the end of the TAC. To overcome this problem, we use preprocessing of the data. Specifically, we enlarge the original sequence using the last image with activity decreased by a small coefficient. This extension is processed and the results are truncated to the original domain, see Figure 7, right.

Comparison of estimates of the blood tissue is displayed in Figure 8 accompanied by following mean absolute error (MAE) between estimated blood curves and manually obtained blood curve. The BSS+ result (MAE 0.044) is on the top left, the FAROI result (MAE 0.044) is in the top middle, the NMF result (MAE 0.042) is on the top left, the BCMS result (MAE 0.031) is on the bottom left, the S-BSS-vecDC result (MAE 0.015) is on the bottom middle, and the S-BSS-DW result (MAE 0.021) is on the bottom right. All algorithms provide stable estimates of the blood TAC, however the result of the S-BSS-vecDC algorithm are closest to the expected value. All blind source separation algorithms provide slightly lower estimates of the blood TAC than the manual method which could be caused by additional background tissue activity in manually selected ROI of the blood.

## 5. Discussion and Conclusion

In this paper, we review and extend the existing blind source separation algorithms and compare their ability to recover data from dynamic positron emission tomography (PET) where the observed images arise as a superposition of the tissue images. There are six methods in our comparison while three of them assume extended superposition model where activity of each source arise as a convolution between common input and source-specific convolution kernel. In experimental comparison, we focus on clarity of separation

of activity in the blood which could be reliably estimated manually for this data and thus it can be used as a good reference value.

From the results of separation provided by these six methods, we manually selected the sources corresponding to the blood stream and compare their time-activity curves with the manually obtained reference. Our S-BSS-vecDC method [29] outperforms other methods in proximity of its estimates to the reference ones. Agreements of this method with manual selection is very encouraging and has the potential to replace invasive estimation of the blood curve used as the input function in various applications.

**Acknowledgement.** This work was supported by the Czech Science Foundation, grant No. 13-29225S.

## A. Required Probability Distributions

### A.1. Truncated Normal Distribution

Truncated normal distribution, denoted as  $t\mathcal{N}$ , of a scalar variable  $x$  on interval  $[a; b]$  is defined as

$$x \sim t\mathcal{N}(\mu, \sigma, [a, b]) = \frac{\sqrt{2} \exp(-(x - \mu)^2)}{\sqrt{\pi\sigma}(\operatorname{erf}(\beta) - \operatorname{erf}(\alpha))} \chi_{[a,b]}(x), \quad (17)$$

where  $\alpha = \frac{a-\mu}{\sqrt{2\sigma}}$ ,  $\beta = \frac{b-\mu}{\sqrt{2\sigma}}$ , function  $\chi_{[a,b]}(x)$  is a characteristic function of interval  $[a, b]$  defined as  $\chi_{[a,b]}(x) = 1$  if  $x \in [a, b]$  and  $\chi_{[a,b]}(x) = 0$  otherwise.  $\operatorname{erf}()$  is the error function defined as  $\operatorname{erf}(t) = \frac{2}{\sqrt{\pi}} \int_0^t e^{-u^2} du$ . The moments of truncated normal distribution are

$$\hat{x} = \mu - \sqrt{\sigma} \frac{\sqrt{2}[\exp(-\beta^2) - \exp(-\alpha^2)]}{\sqrt{\pi}(\operatorname{erf}(\beta) - \operatorname{erf}(\alpha))}, \quad (18)$$

$$\hat{x^2} = \sigma + \mu\hat{x} - \sqrt{\sigma} \frac{\sqrt{2}[b \exp(-\beta^2) - a \exp(-\alpha^2)]}{\sqrt{\pi}(\operatorname{erf}(\beta) - \operatorname{erf}(\alpha))}. \quad (19)$$

See [27] for multivariate extension.

### A.2. Wishart Distribution

Wishart distribution  $\mathcal{W}$  of the positive-definite matrix  $X \in \mathbf{R}^{p \times p}$  is defined as

$$\mathcal{W}_p(\Sigma, \nu) = |X|^{\frac{\nu-p-1}{2}} 2^{-\frac{\nu p}{2}} |\Sigma|^{-\frac{\nu}{2}} \Gamma_p^{-1}\left(\frac{\nu}{2}\right) \times \exp\left(-\frac{1}{2} \operatorname{tr}(\Sigma^{-1} X)\right), \quad (20)$$

where  $\Gamma_p\left(\frac{\nu}{2}\right)$  is the gamma function. The required moment is:

$$\hat{X} = \nu \Sigma. \quad (21)$$

## References

1. Alf, M., Wyss, M., Buck, A., Weber, B., Schibli, R., Krämer, S.: Quantification of brain glucose metabolism by  $^{18}\text{F}$ -FDG PET with real-time arterial and image-derived input function in mice. *Journal of Nuclear Medicine* 54(1), 132–138 (2013)
2. Bishop, C., Tipping, M.: Variational relevance vector machines. In: Proceedings of the 16th Conference on Uncertainty in Artificial Intelligence. pp. 46–53 (2000)
3. Bodvarsson, B., Hansen, L., Svarer, C., Knudsen, G.: Nmf on positron emission tomography. In: Acoustics, Speech and Signal Processing, 2007. ICASSP 2007. IEEE International Conference on. vol. 1, pp. I–309. IEEE (2007)
4. Calamante, F., Mørup, M., Hansen, L.: Defining a local arterial input function for perfusion mri using independent component analysis. *Magnetic resonance in Medicine* 52(4), 789–797 (2004)
5. Croteau, E., Poulin, E., Tremblay, S., Dumulon-Perreault, V., Sarrhini, O., Lepage, M., Lecomte, R.: Arterial input function sampling without surgery in rats for positron emission tomography molecular imaging. *Nuclear medicine communications* 35(6), 666–676 (2014)
6. Di Paola, R., Bazin, J., Aubry, F., Aurengo, A., Cavailloles, F., Herry, J., Kahn, E.: Handling of dynamic sequences in nuclear medicine. *Nuclear Science, IEEE Transactions on* 29(4), 1310–1321 (1982)
7. Gaujoux, R., Seoighe, C.: Semi-supervised nonnegative matrix factorization for gene expression deconvolution: a case study. *Infection, Genetics and Evolution* 12(5), 913–921 (2012)
8. Germano, G., Chen, B., et al.: Use of the abdominal aorta for arterial input function determination in hepatic and renal pet studies. *Journal of nuclear medicine* 33(4), 613 (1992)
9. Gillis, N.: Successive nonnegative projection algorithm for robust nonnegative blind source separation. *SIAM Journal on Imaging Sciences* 7(2), 1420–1450 (2014)
10. Greuter, H., Boellaard, R., et al.: Measurement of 18f-fdg concentrations in blood samples: comparison of direct calibration and standard solution methods. *Journal of nuclear medicine technology* 31(4), 206–209 (2003)
11. Gunn, R., Gunn, S., Cunningham, V.: Positron emission tomography compartmental models. *Journal of Cerebral Blood Flow & Metabolism* 21(6), 635–652 (2001)
12. Hamill, T., Whitaker, J., Snyder, C.: Distance-dependent filtering of background error covariance estimates in an ensemble kalman filter. *Monthly Weather Review* 129(11), 2776–2790 (2001)
13. Hoyer, P.: Non-negative matrix factorization with sparseness constraints. *The Journal of Machine Learning Research* 5, 1457–1469 (2004)
14. Kim, H., Park, H.: Sparse non-negative matrix factorizations via alternating non-negativity-constrained least squares for microarray data analysis. *Bioinformatics* 23(12), 1495–1502 (2007)
15. Kuruc, A., Caldicott, W., Treves, S.: Improved Deconvolution Technique for the Calculation of Renal Retention Functions. *Comp. and Biomed. Res.* 15(1), 46–56 (1982)
16. Lanz, B., Poitry-Yamate, C., Gruetter, R.: Image-derived input function from the vena cava for 18F-FDG PET studies in rats and mice. *Journal of Nuclear Medicine* 55(8), 1380–1388 (2014)
17. Lee, D., Seung, H.: Algorithms for non-negative matrix factorization. In: Advances in neural information processing systems. pp. 556–562 (2000)
18. Lee, D., Seung, H.: Algorithms for non-negative matrix factorization. In: Advances in neural information processing systems. pp. 556–562 (2001)
19. Liptrot, M., Adams, K., Martiny, L., Pinborg, L., Lonsdale, M., Olsen, N., Holm, S., Svarer, C., Knudsen, G.: Cluster analysis in kinetic modelling of the brain: a noninvasive alternative to arterial sampling. *NeuroImage* 21(2), 483–493 (2004)
20. Liu, R., Jia, J.: Reducing boundary artifacts in image deconvolution. In: Image Processing, 2008. ICIP 2008. 15th IEEE International Conference on. pp. 505–508. IEEE (2008)

21. Miskin, J.: Ensemble learning for independent component analysis. Ph.D. thesis, University of Cambridge (2000)
22. Patlak, C., Blasberg, R., Fenstermacher, J., et al.: Graphical evaluation of blood-to-brain transfer constants from multiple-time uptake data. *J Cereb Blood Flow Metab* 3(1), 1–7 (1983)
23. Riabkov, D., Di Bella, E.: Estimation of kinetic parameters without input functions: analysis of three methods for multichannel blind identification. *Biomedical Engineering, IEEE Transactions on* 49(11), 1318–1327 (2002)
24. Smaragdīs, P.: Non-negative matrix factor deconvolution; extraction of multiple sound sources from monophonic inputs. In: *Independent Component Analysis and Blind Signal Separation*, pp. 494–499. Springer (2004)
25. Šmídl, V., Quinn, A.: *The Variational Bayes Method in Signal Processing*. Springer (2006)
26. Šmídl, V., Tichý, O.: Automatic Regions of Interest in Factor Analysis for Dynamic Medical Imaging. In: *2012 IEEE International Symposium on Biomedical Imaging (ISBI)*. IEEE (2012)
27. Šmídl, V., Tichý, O.: Sparsity in Bayesian Blind Source Separation and Deconvolution. In: Blockeel et al., H. (ed.) *Machine Learning and Knowledge Discovery in Databases (ECML/PKDD 2013)*, Lecture Notes in Computer Science, vol. 8189, pp. 548–563. Springer Berlin Heidelberg (2013)
28. Tichý, O., Šmídl, V.: Kinetic modeling of the dynamic PET brain data using blind source separation methods. In: *Biomedical Engineering and Informatics (BMEI), 2014 7th International Conference on*, pp. 329–334. IEEE (2014)
29. Tichý, O., Šmídl, V.: Bayesian blind separation and deconvolution of dynamic image sequences using sparsity priors. *Medical Imaging, IEEE Transaction on* 34(1), 258–266 (January 2015)
30. Tichý, O., Šmídl, V.: Non-parametric bayesian models of response function in dynamic image sequences. Pre-print submitted to *Computer Vision and Image Understanding* (2015), (arXiv:1503.05684 [stat.ML])
31. Tichý, O., Šmídl, V., Šámal, M.: Model-based extraction of input and organ functions in dynamic scintigraphic imaging. *Computer Methods in Biomechanics and Biomedical Engineering: Imaging & Visualization* (2014), (in print, doi:10.1080/21681163.2014.916229)
32. Zhou, S., Chen, K., Reiman, E., Li, D., Shan, B.: A method of generating image derived input function in quantitative 18F-FDG PET study based on the monotonicity of the input and output function curve. *Nuclear medicine communications* 33(4) (2012)

**Ondřej Tichý** is Ph.D. student at the Institute of Information Theory and Automation, Czech Academy of Sciences. He obtained a B.Sc. and M.Sc. degree in computer sciences from Faculty of Nuclear Sciences and Physical Engineering in 2008 and 2010 respectively. He obtained the Werner von Siemens Excellence Award for his master thesis in 2010 and the Rektorys Award in Applied Mathematics in 2012 and 2014. He is an author or co-author of several conference and journal papers focused on automated analysis in dynamic medical imaging and the problem of Bayesian blind source separation.

**Václav Šmídl** received the masters degree in Control Engineering from the University of West Bohemia (UWB), Pilsen, Czech Republic in 1999, and the Ph.D. degree in Electrical Engineering from Trinity College Dublin, Ireland in 2004. Since 2004, he has been a researcher in the Institute of Information Theory and Automation, Prague, Czech Republic. In October 2010 he joined the Regional Innovation Centre for Electrical Engineering, RICE. His research interests are advanced estimation and control techniques and their applications. He published one research monograph, 13 journal papers and over 50 conference papers.

*Received: December 1, 2014; Accepted: August 1, 2015.*

